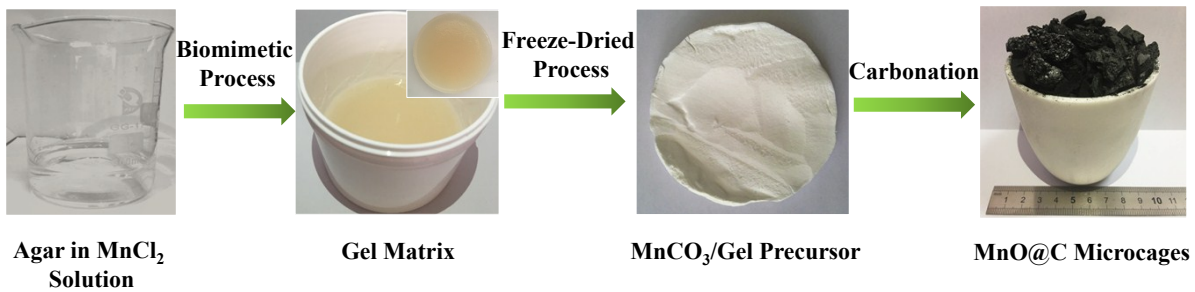


# High Performance MnO@C Microcages with a Hierarchical Structure and Tunable Carbon Shell for Efficient and Durable Lithium Storage

*Chuanxin Hou,<sup>1,2</sup> Zhixin Tai,<sup>3</sup> Lanling Zhao,<sup>4</sup> Yanjie Zhai,<sup>1</sup> Yue Hou,<sup>1</sup> Yuqi Fan,<sup>2</sup> Feng Dang,<sup>1\*</sup> Jun Wang<sup>1\*</sup> and Huakun Liu<sup>3\*</sup>*

1. *Key Laboratory for Liquid-Solid Structural Evolution and Processing of Materials (Ministry of Education), Shandong University, Jinan 250061, P.R. China*
2. *Institute of Environment and Ecology, Shandong Normal University, Jinan 250014, China*
3. *Institute for Superconducting and Electronic Materials, University of Wollongong, Wollongong, NSW 2522, Australia*
4. *School of Physics, Shandong University, Jinan, 250100, P.R. China*

*E-mail:* [dangfeng@sdu.edu.cn](mailto:dangfeng@sdu.edu.cn)



**Figure S1.** Schematic illustration of preparing MnO@C microcages.

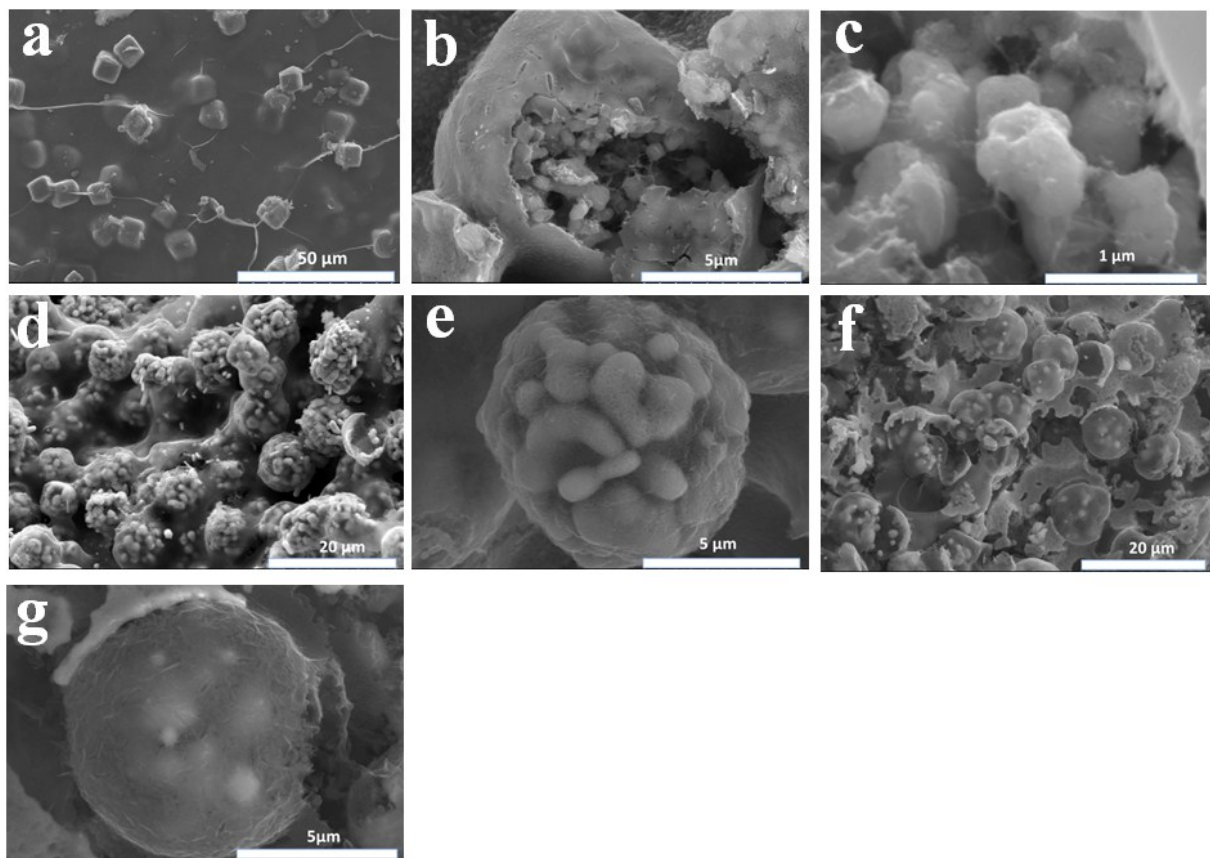


**Figure S2.** SEM images of MnCO<sub>3</sub> precursor particles (a), MnO@C-700 (b,c), MnO@C-900 (d, e) and MnO@C-1100 (f, g).

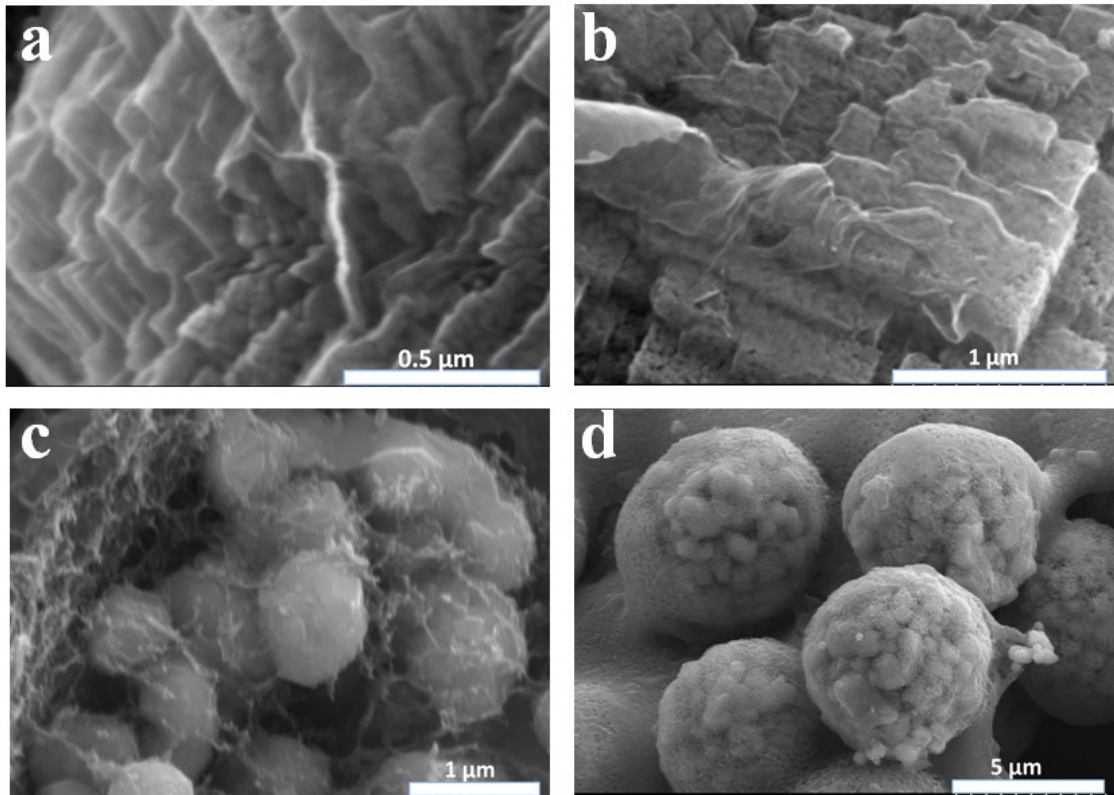


**Figure S3.** SEM image of the MnCO<sub>3</sub> processor contained graphene (0.9 wt%) (a, b), MnO@C-G9-700 contained graphene (c) and MnO@C-G12 microcage (d).

The formation mechanism and structure of biomimetic synthesized rhombohedral MnCO<sub>3</sub> particles have been studied and introduced by Oaki and Liu et al.<sup>1-3</sup> In the biomimetic process for the synthesis of MnCO<sub>3</sub>, the rhombohedral MnCO<sub>3</sub> particles have a mesocrystal structure, in which small crystalline units grow in organic agar matrix and oriented aggregate into an organic-inorganic composite large particle. At the first stage, through the diffusion of CO<sub>2</sub> into the agar gel matrix, MnCO<sub>3</sub> nanocrystals grow and homogenously disperse in the organic matrix. Agar gel matrix will hinder the diffusion of nanocrystals. In the following stage, the nanocrystal will homoepitaxially aggregate rather than the classic atom-by-atom growth in the initial process due to the low initial adhesion force or energy, and the nanocrystal have sufficient time and freedom to align up epitaxially before irreversibly bounded together, finally forming the rhombohedral particles. The biological macromolecules play an important

role for the morphogenesis of MnCO<sub>3</sub> mesocrystals. Different macromolecules result into different morphologies of the MnCO<sub>3</sub> mesocrystals.

1. Y. Oaki, A. Kotachi, T. Miura, H. Imai, *Adv. Funct. Mater.*, **2006**, *16*, 1633-1639.
2. T. Kokubu, Y. Oaki, E. Hosono, H. Imai, *Adv. Funct. Mater.*, **2011**, *21*, 3673-3680.
3. C. F. Liu, C. K. Zhang, H. Q. Song, G. P. Zhang, Y. G. Liu, X. H. Nan, G. Z. Cao, *Nano Energy*, **2016**, *22*, 290-300.

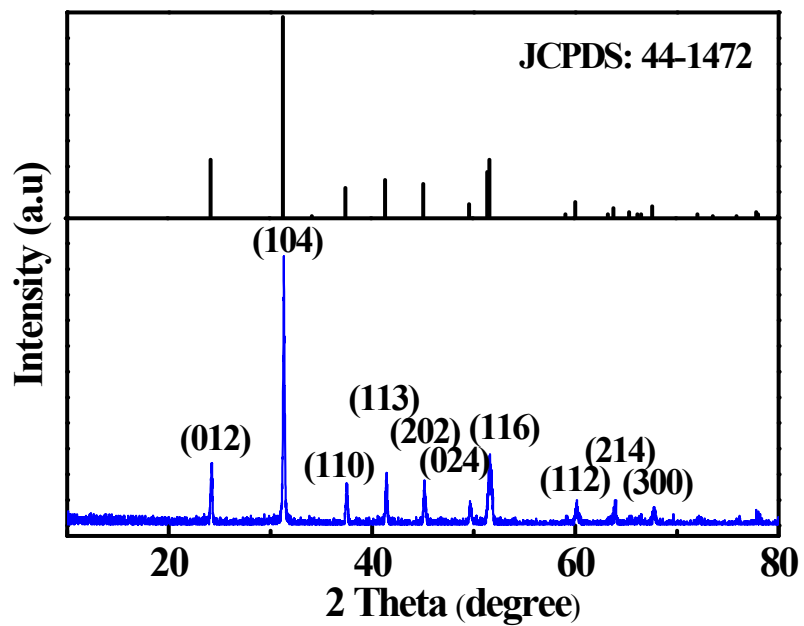


**Figure S4.** XRD pattern of MnCO<sub>3</sub>/gel precursor.

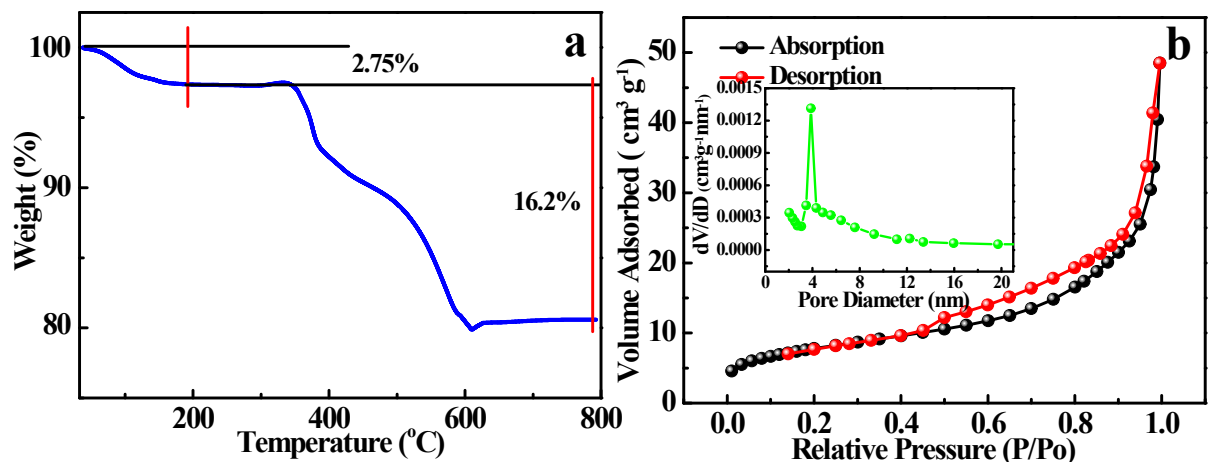


**Figure S5.** TGA curve of MnO@C-700 (a); nitrogen adsorption-desorption isotherm loop and pore size distribution curve calculated from desorption branch by the BJH model of MnO@C-700 (b).

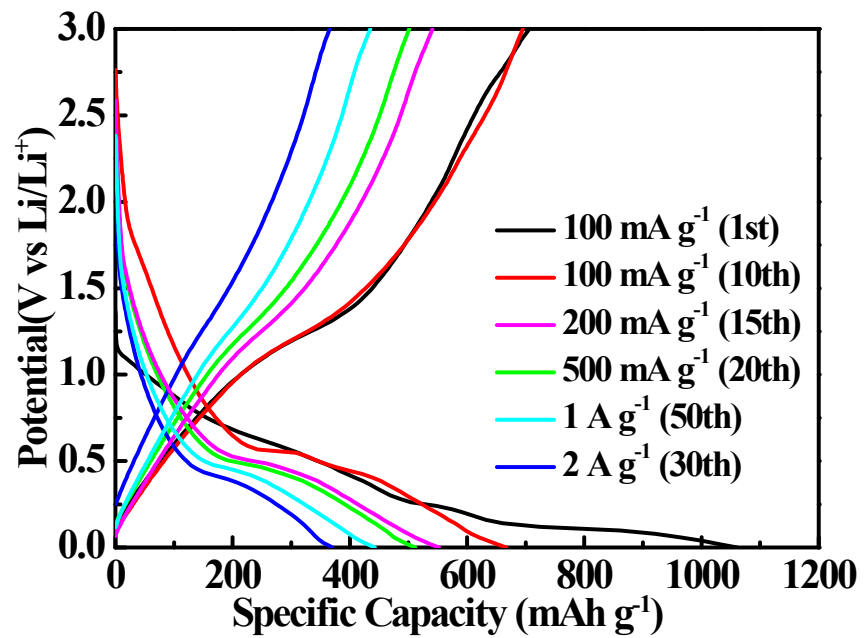


**Figure S6.** Charge-discharge profiles of MnO@C-700 electrodes at different current densities.

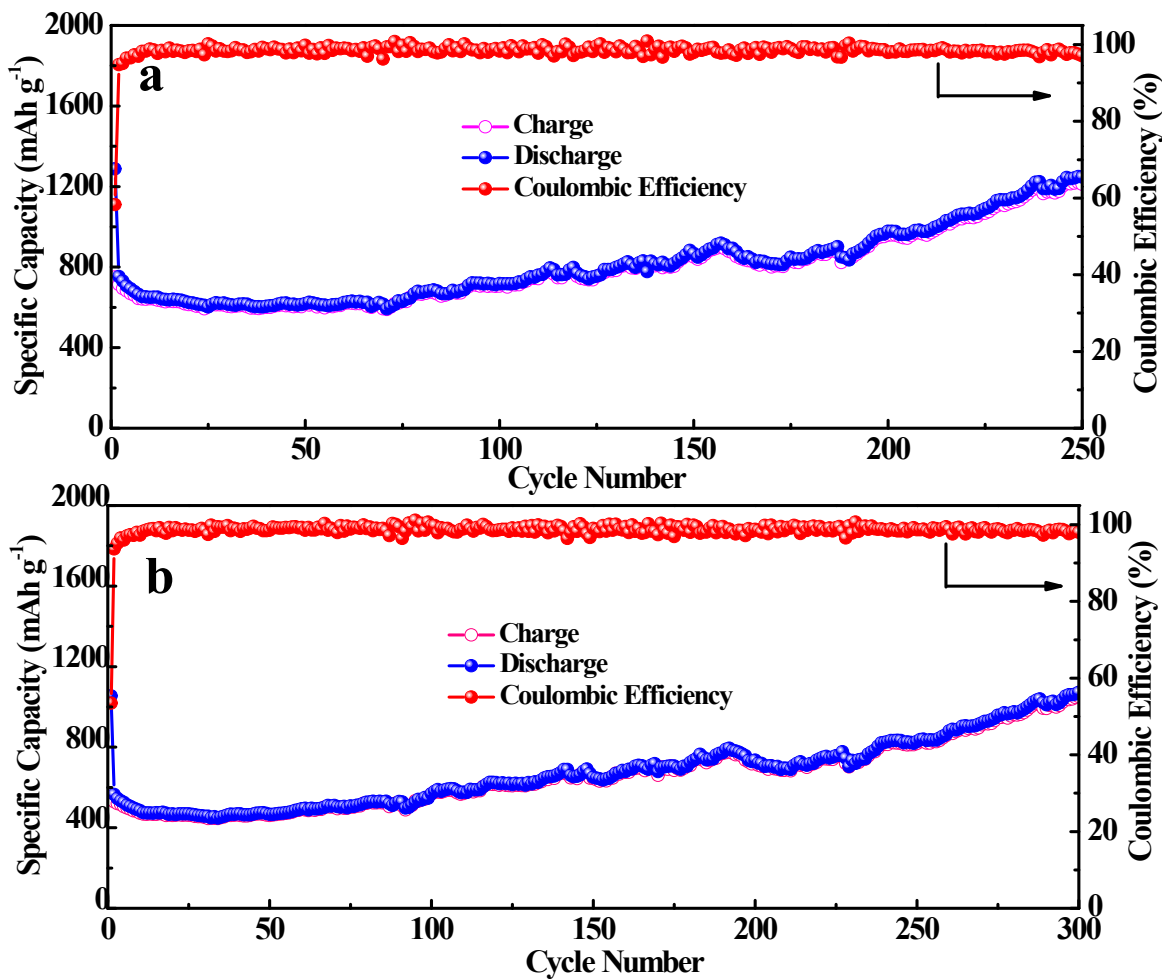


**Figure S7.** Cycling performance and coulombic efficiencies of MnO@C-900 (a) and MnO@C-1100 (b) electrodes at  $0.1 \text{ A g}^{-1}$ .

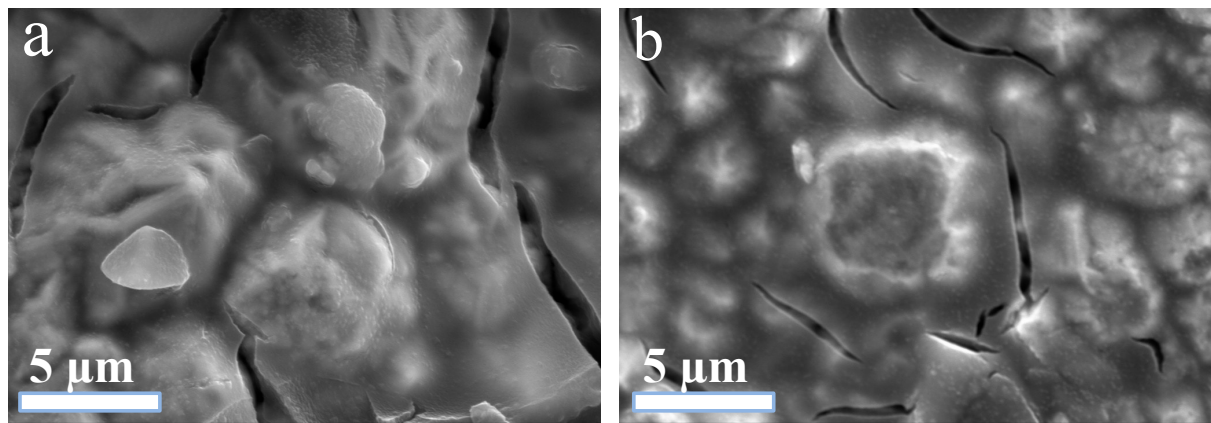


**Figure S8.** SEM images of MnO@C-900 (a) and MnO@C-1100 (b) electrodes after 250, 300 cycles, respectively, at  $0.1 \text{ A g}^{-1}$ .

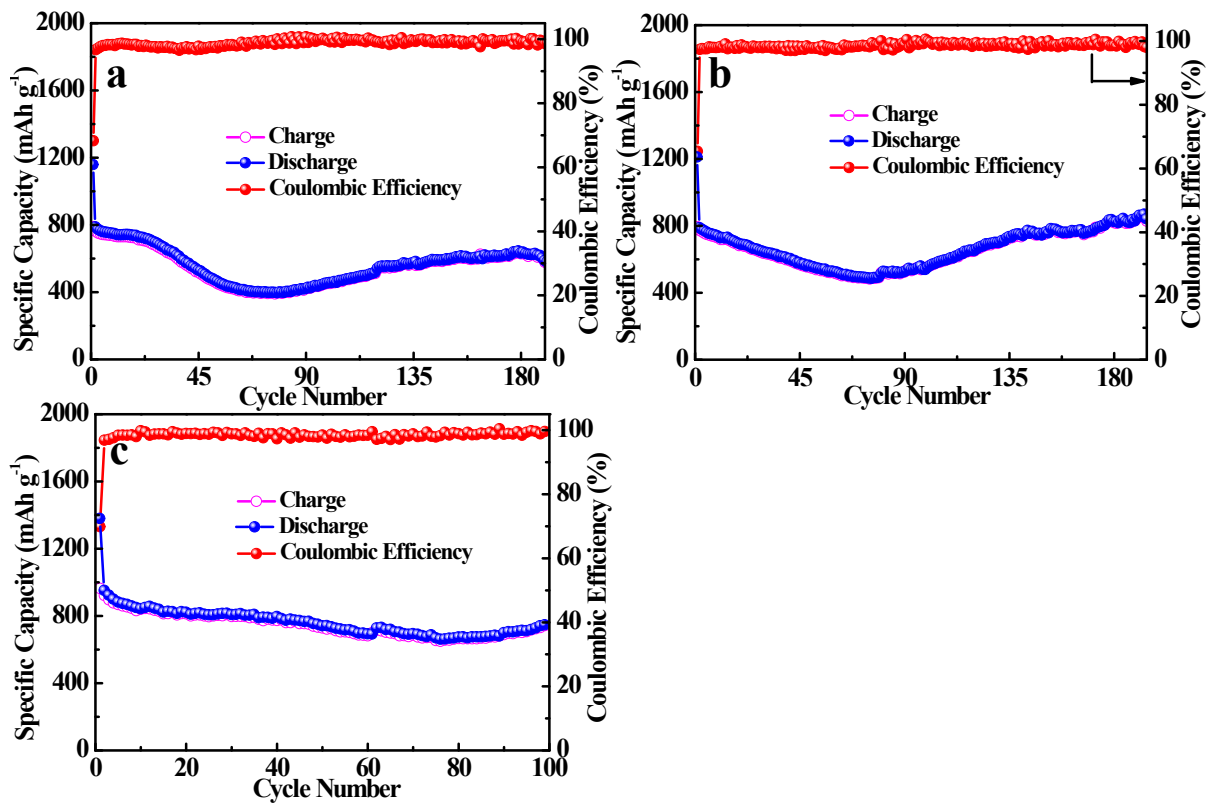


**Figure S9.** Cycling performance and coulombic efficiencies of  $\text{MnO}@\text{C-G3-700}$  (a),  $\text{MnO}@\text{C-G6-700}$  (b) and  $\text{MnO}@\text{C-G12-700}$  electrodes at  $0.1 \text{ A g}^{-1}$ .

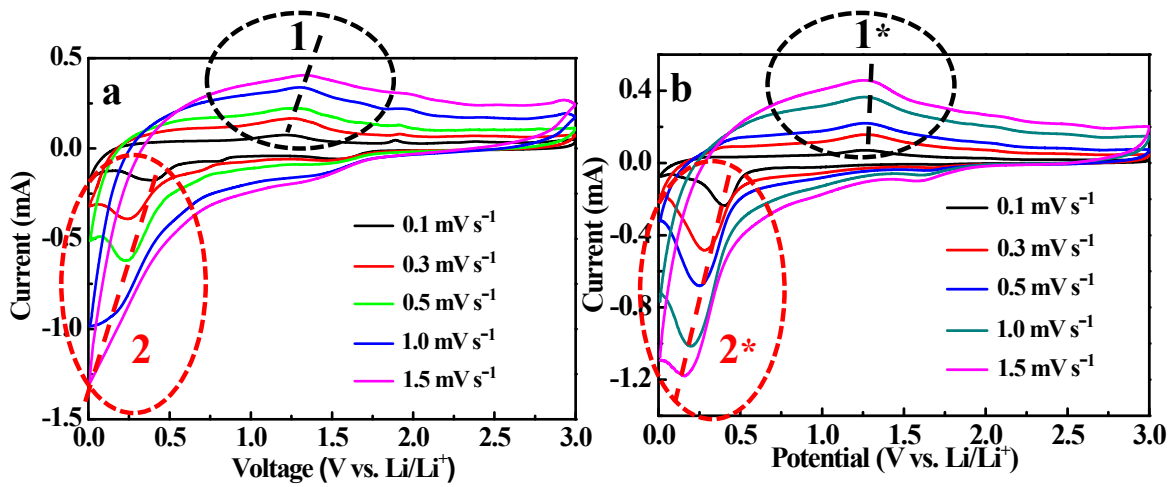


**Figure S10.** CV curves at different scan rates from  $0.1\text{--}1.5\text{ mV s}^{-1}$  of MnO@C-700 (a) and MnO@C-G9-700 (b) electrodes.

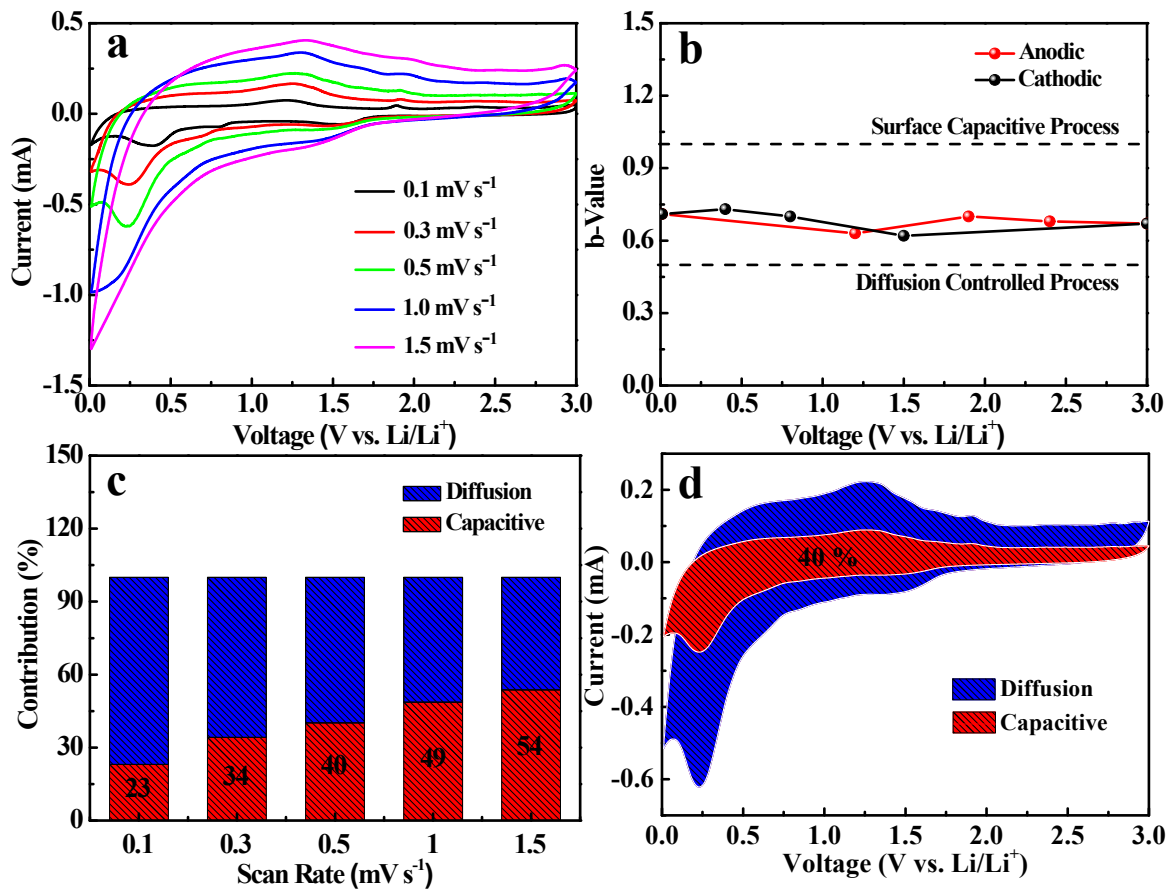


**Figure S11.** Kinetic analysis of the electrochemical behaviors of MnO@C-700 electrode: CV curves at different scan rates from 0.1-1.5 mV s<sup>-1</sup> (a); b-values plotted against different battery potentials (b); the ratio of capacitive and diffusion contribution at different scan rates (c); the capacitive contribution to charge storage at scan rate of 0.5 mV s<sup>-1</sup> (d).

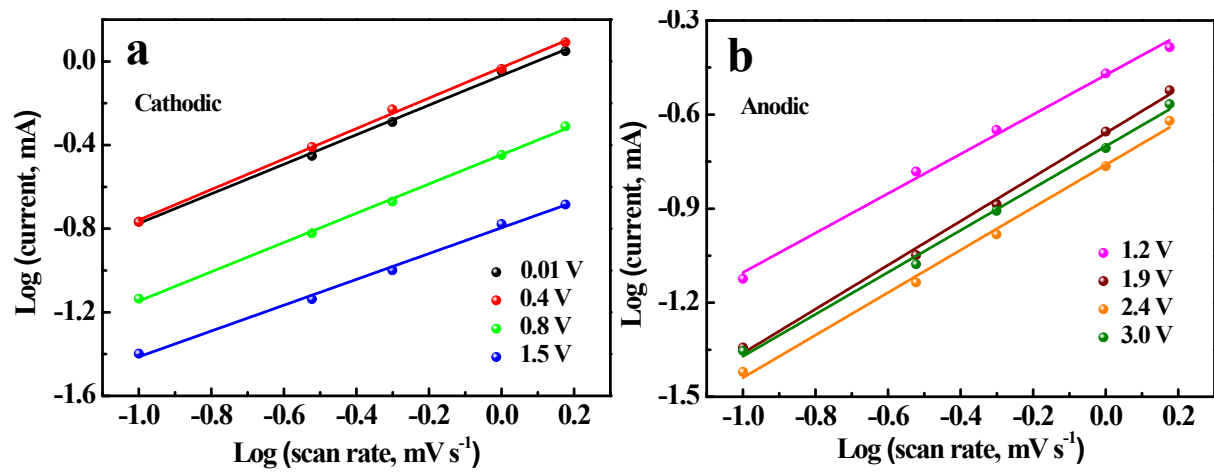


**Figure S12.** Current responses plotted against different scan rates of  $\text{MnO}@\text{C-700}$  electrodes at different potentials for cathodic scans (a) and anodic scans (b).

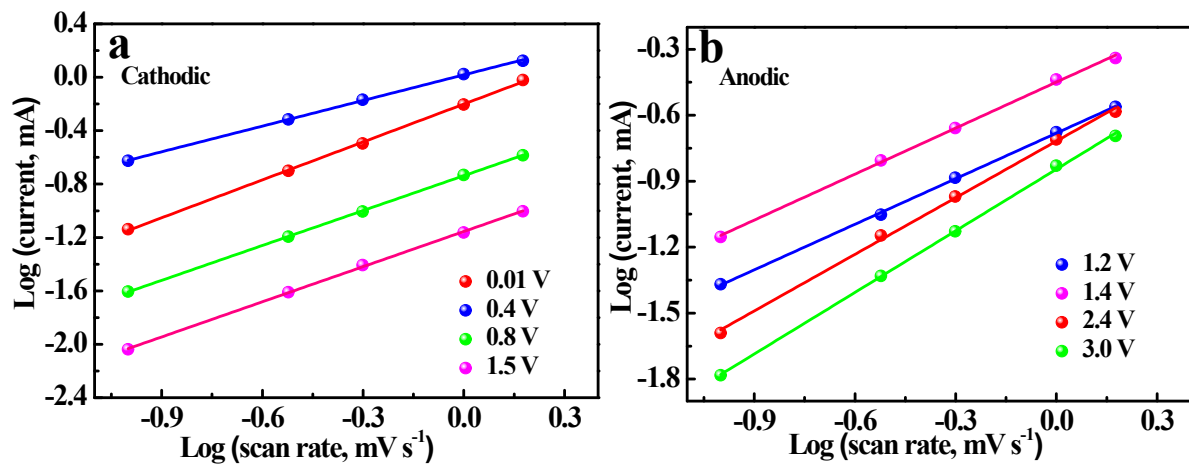


**Figure S13.** Current responses plotted against different scan rates of  $\text{MnO}@\text{C-G9-700}$  electrodes at different potentials for cathodic scans (a) and anodic scans (b).